AGU PUBLICATIONS

JGR

Journal of Geophysical Research: Earth Surface

RESEARCH ARTICLE
10.1002/2016JF003887

The dynamics of surges in the 3 February 2015 avalanches in Vallée de la Sionne

A. Köhler[1], J. N. McElwaine[2], B. Sovilla[1], M. Ash[3], and P. Brennan[3]

[1]WSL Institute for Snow and Avalanche Research SLF, Davos Dorf, Switzerland, [2]Department of Earth Sciences, Durham University, Durham, UK, [3]Department of Electronic and Electrical Engineering, University College London, London, UK

Key Points:
- An avalanche's mass can increase many times by secondary releases, which gives rise to major surges
- Internal surges frequently overtake the leading edge
- The effective friction varies dramatically between inside the flow and the leading edge

Correspondence to:
A. Köhler,
koehler@slf.ch

Citation:
Köhler, A., J. N. McElwaine, B. Sovilla, M. Ash, and P. Brennan (2016), The dynamics of surges in the 3 February 2015 avalanches in Vallée de la Sionne, *J. Geophys. Res. Earth Surf.*, *121*, 2192–2210, doi:10.1002/2016JF003887.

Received 15 MAR 2016
Accepted 17 OCT 2016
Published online 22 NOV 2016

Abstract Five avalanches were artificially released at the Vallée de la Sionne test site in the west of Switzerland on 3 February 2015 and recorded by the GEOphysical flow dynamics using pulsed Doppler radAR Mark 3 radar system. The radar beam penetrates the dilute powder cloud and measures reflections from the underlying denser avalanche features allowing the tracking of the flow at 111 Hz with 0.75 m downslope resolution. The data show that the avalanches contain many internal surges. The large or "major" surges originate from the secondary release of slabs. These slabs can each contain more mass than the initial release, and thus can greatly affect the flow dynamics, by unevenly distributing the mass. The small or "minor" surges appear to be a roll wave-like instability, and these can greatly influence the front dynamics as they can repeatedly overtake the leading edge. We analyzed the friction acting on the fronts of minor surges using a Voellmy-like, simple one-dimensional model with frictional resistance and velocity-squared drag. This model fits the data of the overall velocity, but it cannot capture the dynamics and especially the slowing of the minor surges, which requires dramatically varying effective friction. Our findings suggest that current avalanche models based on Voellmy-like friction laws do not accurately describe the physics of the intermittent frontal region of large mixed avalanches. We suggest that these data can only be explained by changes in the snow surface, such as the entrainment of the upper snow layers and the smoothing by earlier flow fronts.

1. Introduction

Avalanches are a major natural hazard in mountainous regions. They kill hundreds of people a year and cause significant economic damage. In Europe, the main means of risk mitigation are hazard zoning and forecasting. These are largely based on a combination of historical records, numerical simulations, and expert judgements [*Eckert et al.*, 2012].

To draw up hazard maps, predictions of runout distances, flow velocities, and impact pressures based on numerical simulations of avalanches are necessary. Even though the first avalanche models were developed more than 60 years ago, they are still based on simple assumptions [*Ancey*, 2006; *Issler et al.*, 2005]. The parameters for these avalanche models are chosen by fitting predicted runout distances to measurements of the deposits using photogrammetry or other means. The avalanche propagation models are then used to predict the flow thickness and velocity, which is then used as an input to calculate impact forces from empirical relations [*Sovilla et al.*, 2016]. A characteristic of the implementation of most models is that they are highly dissipative resulting in smooth velocity and height fields that are typically largest at the front and do not contain roll waves or internal surges.

Measurements performed inside the flow, however, indicate that the maximum avalanche velocities can occur well behind the leading edge. The structure of the flow is thus far more complex than previously thought [*Sovilla et al.*, 2015]. Figure 1b shows a schematic of a large mixed powder avalanche with the three main regions delineated. *Sovilla et al.* [2015] showed direct evidence for an intermittent frontal region from density and impact pressure measurements. This region is characterized by a relatively low volume fraction with sporadic high-density clusters of snow (Figure 1a and red vertical bars in Figure 1b). This region can reach approximately as much as 300 m into the flow until the "classical" dense core begins. The dense core, a flowing, continuously high-density region, then extends to the tail of the avalanche. For large avalanches the intermittent region and the dense flow are usually covered by a powder cloud, which has low density and consists of single snow grains [*Rastello et al.*, 2011] suspended against gravity by turbulence and can develop if the

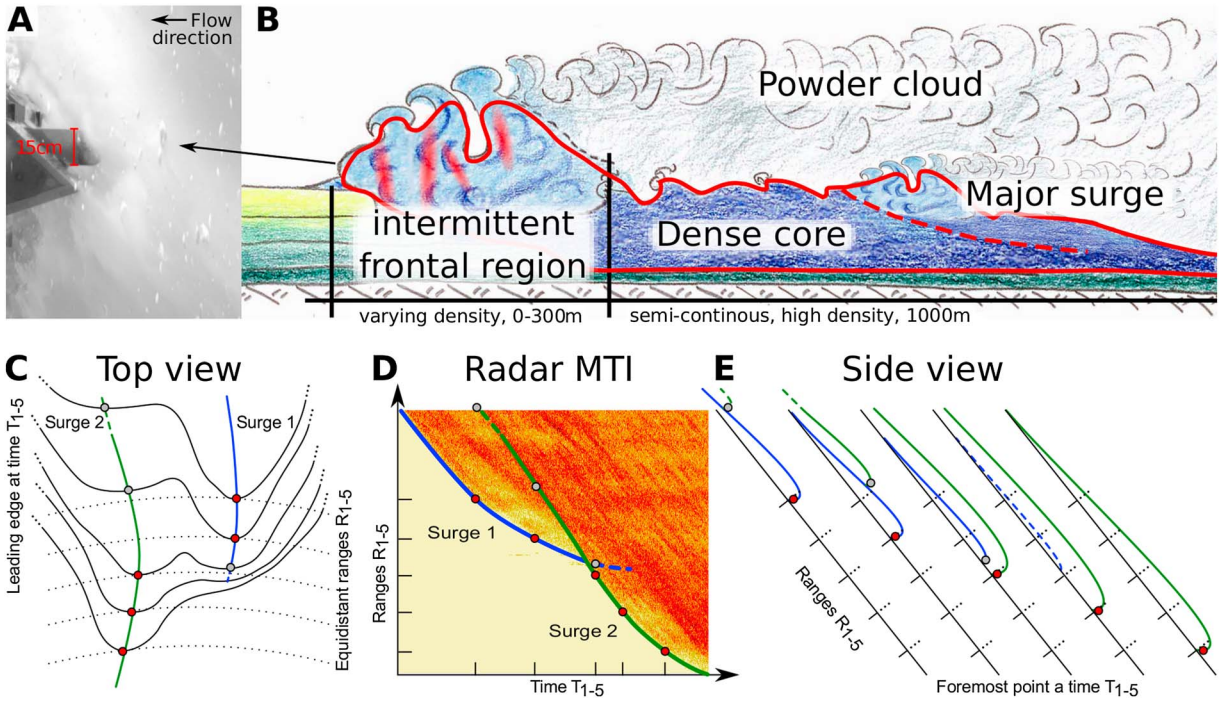

Figure 1. (a) Picture of leading edge of avalanche #0017 reaching the instrumented pylon. The steel wedge points against the flow. The cylindrical pressure sensor at 5.5 m above the ground acts as a scale of 15 cm diameter. The visible snow clumps are big enough to be detected by the radar. (b) Schematic drawing of an avalanche from *Sovilla et al.* [2015] containing the intermittent frontal region and the dense core obscured by a powder cloud. The red line outline indicates the denser flow regions which give reflections to the radar signal. (c) A plan view with contours of the avalanche's leading edge showing how surge 1 could be overtaken by surge 2 laterally. (d) Ambiguous MTI plot of two crossing surges; dots correspond to sketch left and right. (e) Side view of surge 2 overtaking and covering surge 1 on the same talweg.

Richardson number is low enough [see *Turnbull et al.*, 2007; *Carroll et al.*, 2013, and references therein]. A similar picture of these three regions was proposed first by *Schaerer and Salway* [1980] from observations in Roger's pass. They note the work of *Te Chow* [1959] on open channel flow that states Vedernikov's criterion that for Froude numbers >2 a "slug flow" regime develops from a dense flow having an unstable surface characterized by surges and turbulent ridges separated by highly agitated regions and that for Froude numbers >3.5 [*Henderson*, 1966] air entrainment leads to the occurrence of a middle zone, they call "light flow." *Hopfinger* [1983] proposed a similar idea that roll waves with strong air intake are regions of turbulences with roller motion and may be the cause of the powder cloud. This and the light flow are probably equivalent to our intermittent frontal region.

Detailed measurements on full-scale avalanches are very rarely available, notably from point measurements in Vallée de la Sionne test site (VdlS) [*Sovilla et al.*, 2013]. However, these measurements are only performed at a single point on the slope and may not represent the spatial behavior of the flow. Filming and photography can give information over the whole slope, but most of the complex flow structures and dynamically relevant processes happen below the powder cloud and are optically obscured. This makes it difficult to observe the evolution of such structures and to investigate how they affect the avalanche's dynamics.

To obtain spatial data on the dynamic features inside the avalanche, GEOphysical flow dynamics using pulsed Doppler radAR (GEODAR), a novel avalanche radar, was developed by *Ash et al.* [2010] and installed at Vallée de la Sionne test site in the winter season 2010–2011 [*Sovilla et al.*, 2013]. With the first setup, referred to as Mark 1, two natural released avalanches were analyzed [*Vriend et al.*, 2013]. For the winter season 2012/2013, the system hardware was improved using better cabling, phase synchronization, and antenna placement. The improved system is referred to as Mark 3. The software for the data processing has since been further developed to improve noise reduction, filtering, and normalization.

One of the major problems in interpreting GEODAR data in the past was the lack of measurements for comparison. Until 2015, only naturally released avalanches were observed with GEODAR. No additional spatial data,

such as video or laser scan, were available as such data are only captured with artificial releases. Moreover, with natural releases, the data sets are frequently incomplete since the radar measurement is only started when the avalanche has reach a certain speed and size for the seismic sensors to trigger the data acquisition.

The avalanches described here were released artificially, and the radar acquisition started manually before the release, so that the whole avalanche event could be captured from initiation to deposition. High-definition video recordings, laser scans, and flow height data were obtained for the avalanches from before the release until the whole avalanche stopped as well. We combine these data sets to gain a very detailed and consistent image of the denser parts of the flow, which indicates that the avalanche's dynamics are influenced by numerous surges. The resulting data set provides a great opportunity to better understand the radar images and thus the avalanche's surge dynamics.

In this paper we define the "leading edge" of the avalanche as the lower edge of the moving snow on the terrain. The top view in Figure 1c draws the leading edge as one of the black lines which can be made up of several surges. The "front" of a surge is then the closest point (red and gray dots) to the radar along the talweg, which is the steepest descent path down the digital terrain model. The procedure to convert the radar range $r(t)$ into arc-length coordinates $s(t)$ down the talweg is described in section 2.1. Similarly, we define the "approach velocity" as the speed of a flow feature along the line of sight $\dot{r}(t)$, whereas "velocity" refers to the ground-parallel velocity down the talweg $\dot{s}(t)$.

The paper will begin by introducing the measurement devices used in this paper: the GEODAR radar system, the flow height measuring frequency-modulated, continuous wave (FMCW) radars, the video recording cameras, and the laser scan system. In section 3.1 we show that the GEODAR system is able to detect flow height variation in the avalanche which we will call surges. In section 3.2 we further divide these surges into larger "major" and smaller "minor" surges and give explanations about their origin and their velocity (section 3.3). The discussion in section 4 is mainly divided into the effect of both types of surges on the avalanche's movement.

2. Method and Data

Five avalanches were artificially released at the Vallée de la Sionne (VdlS) test site [*Ammann*, 1999] in Canton Valais, Switzerland, on 3 February 2015; see Figure 2 for a map. The avalanches were observed on the east facing slope, which has an elevation drop of around 1300 m. The release area is around 2 km wide and consists of steep slopes of 35° to 45°. The release area is divided into three different zones which are named Pra Roua, Crêta Besse 1, and Crêta Besse 2 from south to north (or from left to right when looking at the slope). The middle section of the face contains two main couloirs, which tend to channel the avalanches. Avalanches from Pra Roua and Crêta Besse 1 mostly flow down Channel 1, whereas avalanches from Crêta Besse 2 flow down Channel 2. Both avalanches presented here are released in Crêta Besse 1.

The Crêta Besse 1 path is equipped with sensors at three different locations: cavern A at 2250 m above see level (asl), cavern B at 1890 m asl, and a 20 m tall pylon at 1640 m asl. Upward looking radar systems [*Gubler and Hiller*, 1984] and seismic sensors [*Pérez-Guillén et al.*, 2015], which trigger the automatic recording, are installed in caverns A and B. The pylon is equipped with sensors at different heights. These measure flow height, impact pressure, air pressure, velocity, density, and temperature [*Sovilla et al.*, 2013]. The GEODAR radar system, which is the main data source in this publication, is mounted in a bunker 40 m up the counter slope at 1485 m asl facing the slope (CH1903 coordinates: N595 246 m, E126 706 m).

2.1. GEODAR

GEODAR (GEOphysical flow dynamics using pulsed Doppler radAR) is a frequency-modulated, continuous wave phased-array radar system. The radar is able to resolve the range, the Doppler velocity, and the lateral position of a reflecting target; however, here we only use the range data. A detailed description of the measurement principle and the radar design can be found in *Ash et al.* [2010, 2011]. The first published results were based on findings with GEODAR Mark 1 [*Vriend et al.*, 2013], whereas the data described here were obtained with the GEODAR Mark 3 system. This system has a higher pulse repetition rate, which increases the measurement frequency, and has a better pulse-to-pulse coherency due to the use of phase-locked signals which results in a stable phase between each pulses and each antenna. Furthermore, larger high-speed storage extends the capture time to 9 min and low-loss cables provide a higher signal-to-noise ratio. All references to GEODAR in the rest of the paper refer to the Mark 3 system.

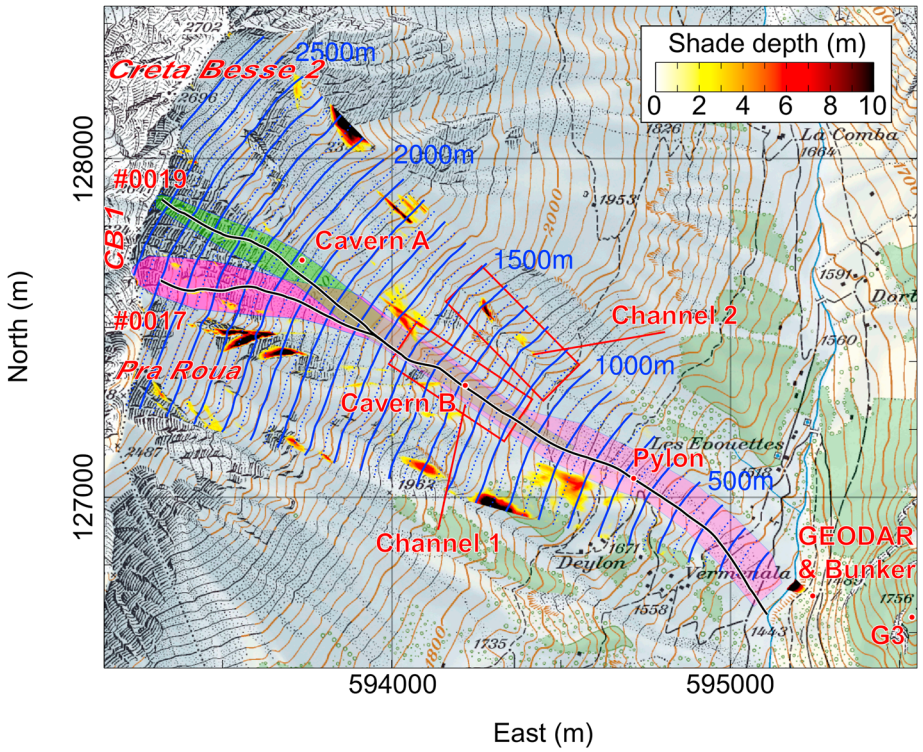

Figure 2. Overview of the Vallée de la Sionne (VdlS) test site. Blue contour lines cover the area observed by GEODAR and indicate the radar range (distance from bunker). Areas not visible to the GEODAR radar are colored with the yellow-black color map indicating the vertical shadow depth. The approximate area of the denser regions of the avalanches is colored violet (#0017) and green (#0019); the corresponding talweg is marked with black lines. Red points mark the locations of the pylon, the caverns, and the bunker hosting the GEODAR system. Original map is obtained from *Swiss Geoportal* [2015] with Swiss coordinate system CH1903 (SRID 21781).

The radar covers nearly the whole slope from the top at range 2700 m to the bottom at range 120 m (Figure 2). The radar collects information over a 30° wide sector, which is averaged over all points at the same line-of-sight distance from the antenna, approximately following the blue contour lines in Figure 2. A complete view of the slope is collected at 111 Hz frame rate with a 0.75 m range resolution. Some regions are shadowed by topographic localized features and cannot be seen by the radar (Figure 2).

Eight receiving antennas are arranged in a sparse-sampled linear array of 8 m base width and collect the avalanche signal. If the data from the eight receivers are postprocessed, the lateral position of the reflectors can be derived using beam-forming techniques [*Ash et al.*, 2014]. Here, however, we averaged the signal of all receivers to improve the signal-to-noise ratio.

The radar operates with a wavelength of 57 mm (5.3 GHz). The radar can see denser parts of the flow-like granules and snow clumps which have an extent larger than the radar wavelength [*Salm and Gubler*, 1985; *Rammer et al.*, 2007]. Such blocks occur in the frontal intermittent region (Figure 1a) as well as in the dense core. The millimeter-sized snow crystals in the powder cloud [*Rastello et al.*, 2011] are too small to reflect the radar signal. Therefore, the powder cloud is expected to be transparent for the radar beam. Not only discrete granules but also changes in dielectric properties in general will alter the radar reflectivity. For the frequency of 5.3 GHz the dielectric properties depend mainly on the density of the air-snow mixture and in case of wet snow on the liquid water content as well [*Hallikainen et al.*, 1986]. Highly varying density and material flowing in localized denser clusters are characteristics for the frontal intermittent region (Figure 1b) [*Sovilla et al.*, 2015], so these flow structures are visible to the radar too.

The penetration depth of electromagnetic waves with a frequency of 5.3 GHz in dry snow is around 10 m [*Rignot et al.*, 2001]. The radar will therefore be able to measure structures throughout the full depth of an avalanche, though the flow surface [*Salm and Gubler*, 1985] where the change in dielectric properties is highest will give the largest signal. Furthermore, the reflected signal contains a large static component from

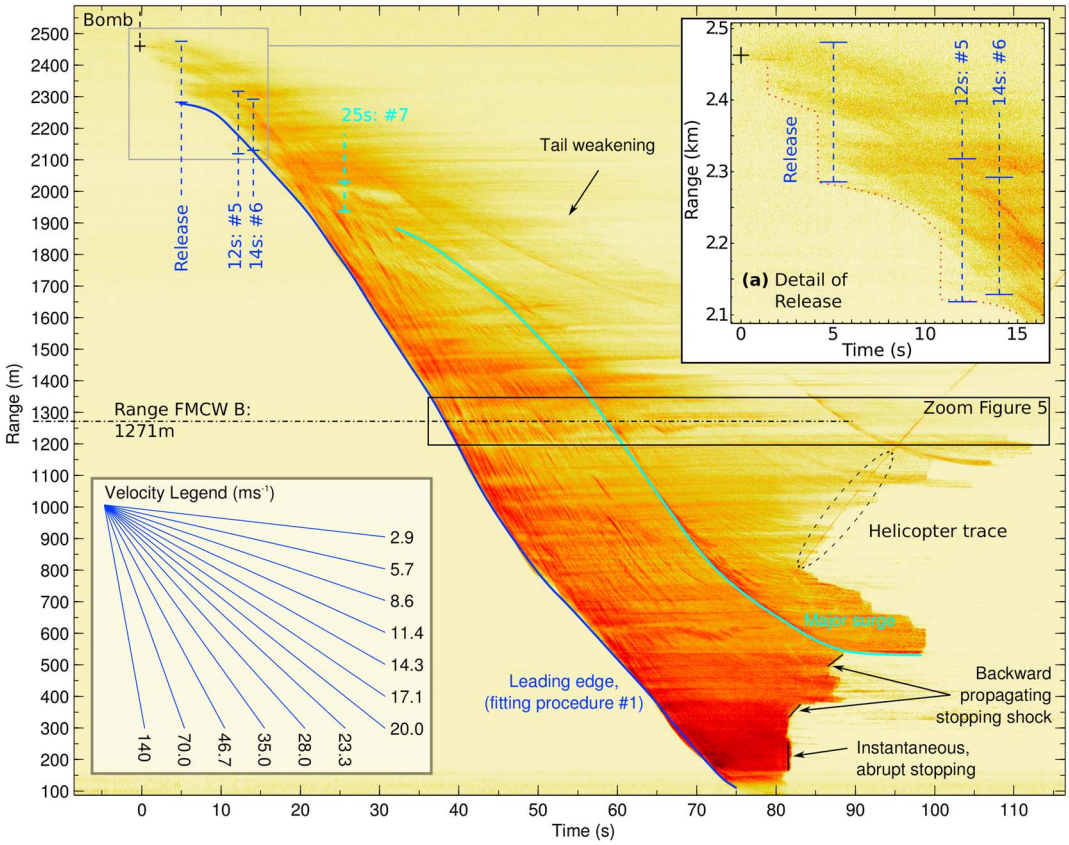

Figure 3. MTI plot of avalanche #0017. Slab releases are highlighted with vertical bars. The most pronounced internal surge and the corresponding slab release is marked with turquoise line. The approach velocity can be inferred from the gradient of the line features. The velocity legend is given for reference. Upper right detail shows slab failures in front of the leading edge as instant jumps forward in range. An in-depth comparison of GEODAR and FMCW B is given in Figure 4 as the detail of the black box.

nonmoving regions of the mountainside. This is removed using a high-pass filter. In the radar community this is known as moving target identification (MTI) since, in the absence of noise, there will be only a signal from moving objects that change their range or change their radar cross section (size and ability to echo radar energy). These MTI plots are space-time plots that show any changes in radar reflectivity at a particular time and range, although the amplitudes of the reflected signal and of the MTI are difficult to interpret directly. MTI plots (Figures 3, 6, and 7) in this paper show signals normalized according to the mean value of the MTI at each range, and the logarithm of the resulting value is mapped with a particular color intensity. We use an MTI high-pass filter of 151 samples in length, with a normalized cutoff frequency of 0.12 generated by the function `fir2.m` in the OCTAVE signal processing package. In contrast to *Vriend et al.* [2013], which applied a time domain filter with coefficients [1, −1] as the difference between only two adjacent pulses, the filter used here has a flatter passband response with a sharper cutoff and gives clearer results.

An MTI plot distinguishes between the moving and nonmoving parts of the slope thus highlighting the avalanche flow (Figure 1d). Yellow or lightly colored parts of the plot indicate areas with no moving snow. The transition to a darker intensity shows the arrival of the avalanche's leading edge. The change in range with time of these edges is the approach velocity that is the velocity on the line of sight toward the radar. Inside the avalanche, the reflectivity constantly changes, giving an MTI signal of medium intensity. Dark lines correspond to surges or waves in the avalanche. Since the plots are averaged across the slope, the lines and edges can cross each other (Figure 1d). They can correspond to features at different lateral locations moving with different speeds (Figure 1c), or they can overtake each other at the same lateral location (Figure 1e). GEODAR cannot distinguish between both cases on its own [*Vriend et al.*, 2013]. Nevertheless, the small powder cloud in the first part of the avalanche track (Figure 5, bottom) allows a degree of visual "calibration" and later in the avalanche path the channeled topography limits the lateral extend of the flow.

Figure 3 shows an MTI plot of a complete avalanche with the avalanche's leading edge marked in blue as the clearest feature. This change from static background to moving snow mostly gives the largest MTI signal. If the flow abruptly stops, the MTI signal is similarly strong, such as at 80 s and 200 m to 400 m range, when the avalanche tail has stopped moving almost instantaneously and the radar signature consists of a vertical stopping edge. A backward propagating stopping shock is observed as rising edge, such as at 87 s and 500 m to 600 m range. In other regions the signal of the avalanche tail is indistinct and the radar signal weakens, e.g., above 1300 m range, as the gradual fading to lighter colors in the plot indicates. This is probably where the avalanche tail slowly comes to a standstill in the steeper regions of the avalanche track. Since the signal quality decreases with the distance from the bunker, the quality of the signal in the release zone is the weakest. Moreover, the signal intensity decreases locally for spots with shadow zones (Figure 2).

Features in the GEODAR data can be tracked to give radar range as a function of time $r(t) = |\mathbf{x}(t) - \mathbf{x}_0|$, where $\mathbf{x}$ is the world coordinates of the feature at time t and $\mathbf{x}_0$ is the coordinate of the GEODAR transmitter at the bunker. A slight adjustment can be made for different receiving antennas and Doppler effects, but these effects are small and thus ignored in this paper. To find $\mathbf{x}(t)$, two additional constraints are needed. One relates to the requirement that the point lies on the terrain surface and the second to the lateral location, which we infer from the laser scan data, the channel topography in the middle section of the path and video observations until the powder cloud gets too opaque as outlined in section 2.3. Once the position is fixed in a talweg, we assume that the feature remains in that talweg.

First, we smoothed the digital terrain model $h(x, y)$ (grid size: 1 m) with a Gaussian filter ($\sigma = 15$ m, kernel size 4σ) since the avalanche is at least this size and will follow a smoothed trajectory. We calculate the talweg, the path of steepest descent, by solving the ordinary differential equation

$$\frac{\mathrm{d}X(s)}{\mathrm{d}s} = -\frac{h_x}{\sqrt{h_x^2 + h_y^2 + 1}}, \tag{1}$$

$$\frac{\mathrm{d}Y(s)}{\mathrm{d}s} = -\frac{h_y}{\sqrt{h_x^2 + h_y^2 + 1}}, \tag{2}$$

with starting positions $X_i(0)$ and $Y_i(0)$. This then produces a set of talwegs in world coordinates $\mathbf{X}_i = \{X_i(s),\ Y_i(s),\ h(X_i(s), Y_i(s))\}$ with $i = 1 \ldots N$, parametrized according to arc length s. The local slope angle is given by $\theta(s) = -\arcsin\left(X'(s)h_x(X(s), Y(s)) + Y'(s)h_y(X(s), Y(s))\right)$, where the subscripts denote the derivative with respect to x or y and $'$ denotes the derivative with respect to s. With the video data we could assign each surge's front to a particular talweg $\mathbf{X}_i(s)$ and then calculated its position, $s(t)$, down the talweg as a function of the radar range $r(t)$, by solving the equation

$$|\mathbf{X}_i(s(t)) - \mathbf{x}_0| = r(t). \tag{3}$$

The ground-parallel velocity of the feature as a function of time is then given by $\dot{s}(t)$ and the corresponding acceleration by $\ddot{s}(t)$. The correction factor from the approach velocity to the ground-parallel velocity is mostly less then 5% to 10% due to the location of GEODAR near the valley bottom. However, numerical differentiation is poorly conditioned and we therefore shall employ a physically based smoothing technique, which we describe later in section 4.2 for calculation of the flow velocity.

2.2. Upward Looking FMCW Radar

Three frequency-modulated, continuous wave (FMCW) radars operate like ground-penetrating radar but point up rather than down [*Gubler and Hiller*, 1984]. They are installed in cavern A below the release area of Crêta Besse 1, cavern B in channel 1, and cavern C close to the instrumented pylon (Figure 2). They can detect layers in the snowpack as well as observe the flowing snow as it passes over them. They give a detailed but qualitative picture of entrainment, deposition, flow height, and flow structure [*Salm and Gubler*, 1985; *Sovilla et al.*, 2006].

The FMCW radars have a vertical resolution of around 100 mm and sample at 40 Hz but perform poorly for wet snow due to the large attenuation. For the avalanches analyzed here, however, the temperatures were so cold that the liquid water content was negligible. The accuracy of the FMCW radars relies on precise snow density information, which affects the speed of microwaves in the snow [*Lundberg et al.*, 2006]. Nevertheless,

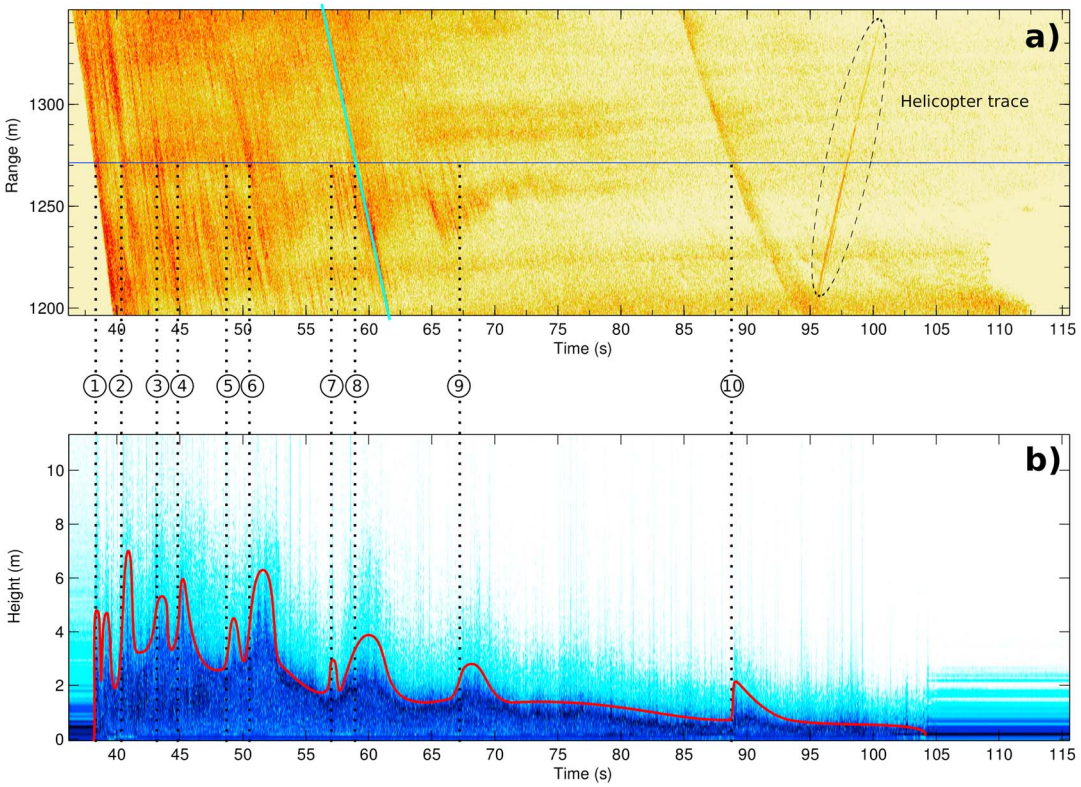

Figure 4. (a) GEODAR data from avalanche #0017 taken at the distance of FMCW B (blue horizontal line at 1271 m range). The turquoise-marked surge from Figure 3 is shown for reference. (b) FMCW flow height data acquired at cavern B. An approximate flow height *h* is drawn in red. Vertical dotted lines help to match flow height variations with GEODAR line features. For detailed description see text. FMCW data are shifted by −1 s relative to GEODAR time due to the transverse displacement of the FMCW system.

they provide an excellent picture of the avalanche structure. The radars are usually used to analyze the snow entrainment by looking at the evolution of the bottom layer of the flow [*Sovilla et al.*, 2015]. Slow basal erosion and a more spontaneous and rapid entrainment of a whole layer of snow can be differentiated [*Sovilla et al.*, 2006]. The FMCW radars are useful in detecting small-scale flow structures that cannot be distinguished in the GEODAR signal since they resolve through the flow rather than across the flow. [*Vriend et al.*, 2013].

Identifying particular features in both the GEODAR and FMCW signals, however, is not straightforward since the avalanches typically have a large lateral extent, and small features will usually not flow directly over the FMCW radars or may even miss them altogether. FMCW B should detect most of the flow height variations because the channeled topography limits the flow width. However, FMCW A is situated in open terrain and the front may pass it well to the side. In this case, traces from particular features may appear later in the local FMCW signal compared with the laterally averaged GEODAR signal, because the FMCW will see the feature after its front has passed.

The time evolutions through the flow height of avalanches #0017 and #0019 are shown in Figures 4 and 6, respectively. The FMCW B data from avalanche #0017 are compared in more depth with the GEODAR data in section 3.1.

2.3. Video

Detailed video recordings were taken from the counter slope at positions known as Plan de Larze (CH1903 coordinates N595 535 m, E126 634 m, and Z1743 m asl) with a high-definition, high frame rate camera. Additional videos were recorded from the bunker. They therefore have exactly the same geometrical perspective as GEODAR and are particularly useful for interpreting the GEODAR data.

The videos allow the tracking of the avalanche's leading edge. For avalanches with a small powder cloud shroud, usually until a certain time after the initiation, the video provides a rare opportunity to visually

corroborate the interpretation of GEODAR's signals. The video recordings are used to infer the lateral position of the avalanches, though usually it is only the powder cloud rather than the denser core.

The camera's geometric and optical parameters are resolved with a set of ground control points, connecting terrain features with the image plain [*McElwaine*, 2003]. The focal length, the camera rotation, and the terrain coordinate of the image centre pixel are inferred by optimizing the match between the control points in the image and the terrain. The video image is registered with a ray tracing technique, resulting in a transfer function between each image pixel and each pixel of the digital terrain model [*Corripio*, 2004]. Thus, information on the terrain, such as elevation and radar ranges, can be transferred into the video images, and features identified in the videos like avalanche contours can be mapped on to the terrain with the reverse transformation.

Another camera is installed 10 m above the ground on the instrumented pylon pointing down toward the sensors. Figure 1a shows the leading of avalanche #0017 hitting the pylon. Once the powder cloud has a certain density, it becomes too opaque for the camera to show much detail.

2.4. Laser Scanning

Three laser scans were taken from a helicopter on the day of the experiments. The equipment and methodology were the same as those used by *Sovilla et al.* [2010]. The first scan was of the undisturbed snow cover before any avalanche was released. The second scan was taken after the first release, just before avalanche #0017 was triggered, and the third scan after all avalanches were released. Five avalanches in total influenced the final pattern of the snow distribution. Several avalanches reached the main runout area making a detailed mass balance for any single event challenging.

The overall snow height distribution is calculated by subtracting the summer digital terrain model from the first laser scan measurements. The net change in the snow cover, indicated by the difference of two consecutive scans, provides information on the erosion and deposition pattern of the avalanches (Figure 5). These volume estimates should be treated carefully where the slope is of medium steepness as erosion may be followed by deposition. In steep respectively shallow slopes, where either erosion or deposition is prevailing, the data are unambiguous [*Sovilla et al.*, 2010]. The net change may be the result of several avalanches especially in the shared runout and channelized parts of the track. The laser scan data are used to infer the release locations and volumes of the secondary released slabs; the values are summarized in Table 1.

2.5. Description of the Avalanches

Five avalanches were artificially released in the VdlS test site on 3 February 2015. During the five preceding days nearly 1 m of new snow had fallen on a 1.35 m thick snow cover with weakly bonded faced crystals on the surface and buried depth hoar layers *WSL Institute for Snow and Avalanche Research SLF* [2015]. The weather station Donin du Jour (2390 m asl) is a few hundred meters north of the test site and is assumed to be representative of the local meteorological conditions. During the snow storm cycle, westerly winds with peak velocities higher than 40 km h^{-1} prevailed. The air temperature stayed below −10°C, preventing the consolidation of the cold new snow and resulting in an unstable snowpack. A thermal camera was used to film the avalanches, and some temperature measurements were also conducted manually in the deposition zone. These showed that the snow temperature in the avalanches at all elevations was at least below −5°C, which meant that the avalanches had a low water content and could be regarded as dry.

The avalanches are classified according to their runout distance [*Pérez-Guillén et al.*, 2015], with avalanches #20150016, #20150017 and #20150020 classified as large and #20150019 and #20150022 classified as medium. Avalanches #20150017 and #20150019 are analyzed in detail in this paper. Figure 2 shows the release areas and the trajectories. We refer to these avalanches by their archive numbers, to allow cross reference with other publications, but the prefix "2015" is excluded in the following sections.

Avalanche #0017 was released at 11:45, from the left side of Crêta Besse 1 (Figure 5, CH1903: N593 273 m, E127 655 m, and Z2574 m asl). The whole avalanche descended through channel 1, flowed over cavern B, and hit the pylon. The initial release volume was not very large (Table 1), but snow entrainment considerably increased the size of the avalanche, resulting in a long runout. The relatively straight trajectory of this avalanche and the high-quality video records make it a perfect test case for analyzing the GEODAR data.

Avalanche #0019 was released at 11:54 in the boundary zone between Crêta Besse 1 and Crêta Besse 2 (Figure 5, CH1903: N593 323 m, E127 876 m, and Z2606 m asl). This medium-sized avalanche flowed over caverns A and B but stopped before reaching the pylon. The small powder cloud, only partly obscured the denser core, and the internal flow structures, allowed a clear comparison between the video data and the

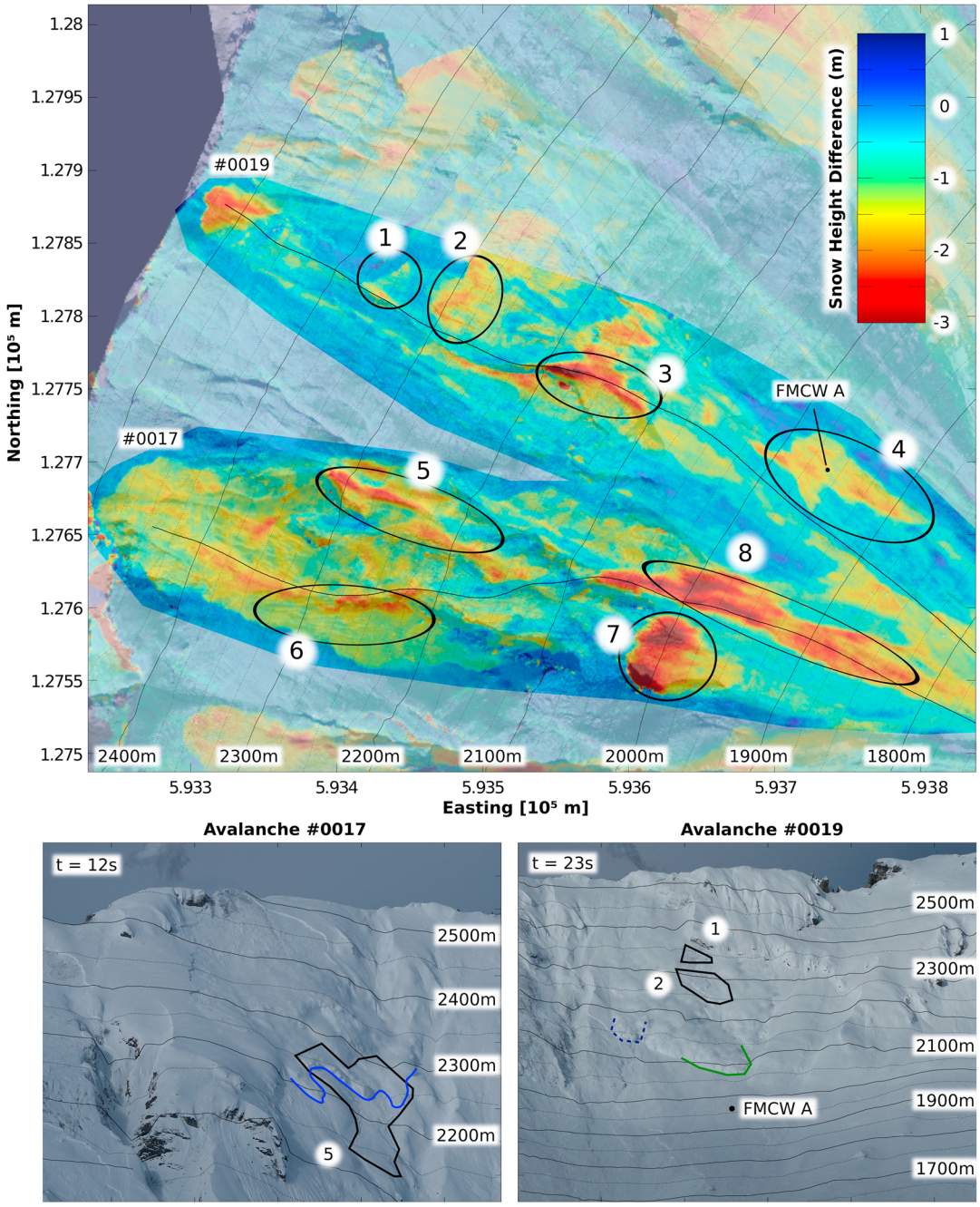

Figure 5. Net changes in the snow cover due to avalanches #0017 and #0019 as the result of the laser scan data. The color scale is limited to 3 m erosion (red) and 1 m deposit (dark blue). (top) Slab release areas are marked with black circles and numbered for easier reference. (bottom) Video snapshots from avalanche #0017 (left) and #0019 (right) at the moment of slab releases (black out line). The contour lines represent the radar range.

GEODAR data. This data set is most interesting for identifying the sources of the avalanche's four major surges and following their evolution along the talweg (Figure 6). The times in all of the figures are relative to the time of the explosions at $t = 0s$ that triggered the avalanches.

3. Major and Minor Surges

3.1. Feature Identification

The main features analyzed in the MTI plots were marked with colored lines in Figures 3 and 6. Such line features correspond to trajectories of features in the flow such as flow fronts, surges, roll waves, or density

Table 1. Location, Time, and Size Parameters of the Slab Releases Identified in Figure 5[a]

	Time (s)	Volume (m^3)	Range (m)	Length (m)	Area (m^2)	Depth (m)
Avalanche #0019		$V_t = 29{,}500$			40,400	0.75
Initial release	3.4	$V_0 = 2{,}200$	2,505	60	1,400	1.55
Slab #1	17.2	$V_1 = 500$	2,355	40	700	0.75
Slab #2	23.4	$V_2 = 3{,}500$	2,285	85	2,800	1.30
Slab #3	20–25[b]	$V_3 = 3{,}300$	2,150	100	1,900	1.80
Slab #4	38.7	$V_4 = 4{,}300$	1,945	155	3,700	1.15
Avalanche #0017		$V_t = 78{,}500$			82,600	0.95
Initial release	5.2	$V_0 = 15{,}200$	2,400	190	13,000	1.15
Slab #5	12.2	$V_5 = 7{,}600$	2,220	200	6,000	1.25
Slab #6	14.1	$V_6 = 5{,}900$	2,215	165	5,900	1.00
Slab #7	25.6	$V_7 = 6{,}300$	1,980	95	3,300	1.90
Slab #8	15–25[b]	$V_8 = 10{,}700$	1,945	255	5,000	2.10

[a]Size parameters are volume, area, and average erosion depth. Outline (area) was carefully picked manually. The accuracy of the depth depends on the laser scanning device, here ±0.05 m, and the volume estimate depends on the area and depth (±5%). Location is given as average radar range and slab length as the extent in range, both with accuracy of around ±5 m.
[b]Time of release roughly estimated.

clusters. These were mapped to the appropriate talweg using the procedure outlined earlier in section 2.1 to obtain the talweg position $s(t)$ as a function of time from the radar range $r(t)$. The velocity derived from these trajectories, $\dot{s}(t)$, is a *phase* velocity rather than a *group* velocity. The group velocity is the velocity of snow granules, whereas the phase velocity is the velocity of flow features. These may be the same if they correspond to the trajectories of blocks of material. They can also be very different since in subcritical regions the phase velocities could be upslope corresponding to backward propagating shocks or roll waves, even though material only moves downslope. Horizontal lines in the MTI are features with zero phase velocity, which may correspond to standing waves. Upward sloping lines are features with negative phase velocity, which may correspond to backward propagating waves or shocks. At the leading edge the phase velocity is the same as the group velocity.

We classify the flow features we track (lines in the MTI) as follows: Those that can be identified as coming from secondary releases (identified from video or laser scan data; see section 3.2) are called *major surges*. These trajectories are nearly all more than 400 m in length; All others are referred to as *minor surges*. These are nearly all shorter than few hundred meters in length. The major surges can start far behind the head but move through the avalanche body and may reach and overtake the head. Several are visible in the MTI plot of avalanches #0017 (Figure 3) and even more in that of #0019 (Figure 6). The minor surges occur in the intermittent frontal region and the dense core but not in the avalanche tail. We believe that the minor surges are most likely internal roll wave-like flow instabilities (see section 3.2).

We define the relative length L_r of a surge as the length of the surge along the talweg L_s divided by the avalanche runout L, the distance between the release and the deposit zone. The major surges (Figures 3 and 6) all have a relative length $l_r = L_s/L$ of higher than 0.4, whereas the minor surges identified in Figure 7 have a relative length of less than 0.2.

The GEODAR data are compared with the FMCW measurements at cavern B for avalanche #0017 in Figure 4. Both data sets are synchronized in time and are displayed above each other. Note that the GEODAR data are displayed as a ±75 m wide section around the range of cavern B, corresponding to the area highlighted by the black box in Figure 3. This simple comparison shows that both minor and major surges in the MTI plot clearly correspond to flow depth variations in the FMCW plot. For example, GEODAR's most pronounced internal feature of avalanche #0017, highlighted in turquoise in Figure 3, corresponds to the flow depth variation #8 in the FMCW B data. Other features, numbered #2, #6, and #10 in Figure 4, also match up nicely with the arrival of the flow height waves at cavern B.

GEODAR reveals many more minor features than FMCW B, possibly because they were relatively small and laterally displaced from cavern B. Thus, their extent must have been smaller than the channel width of 30 m.

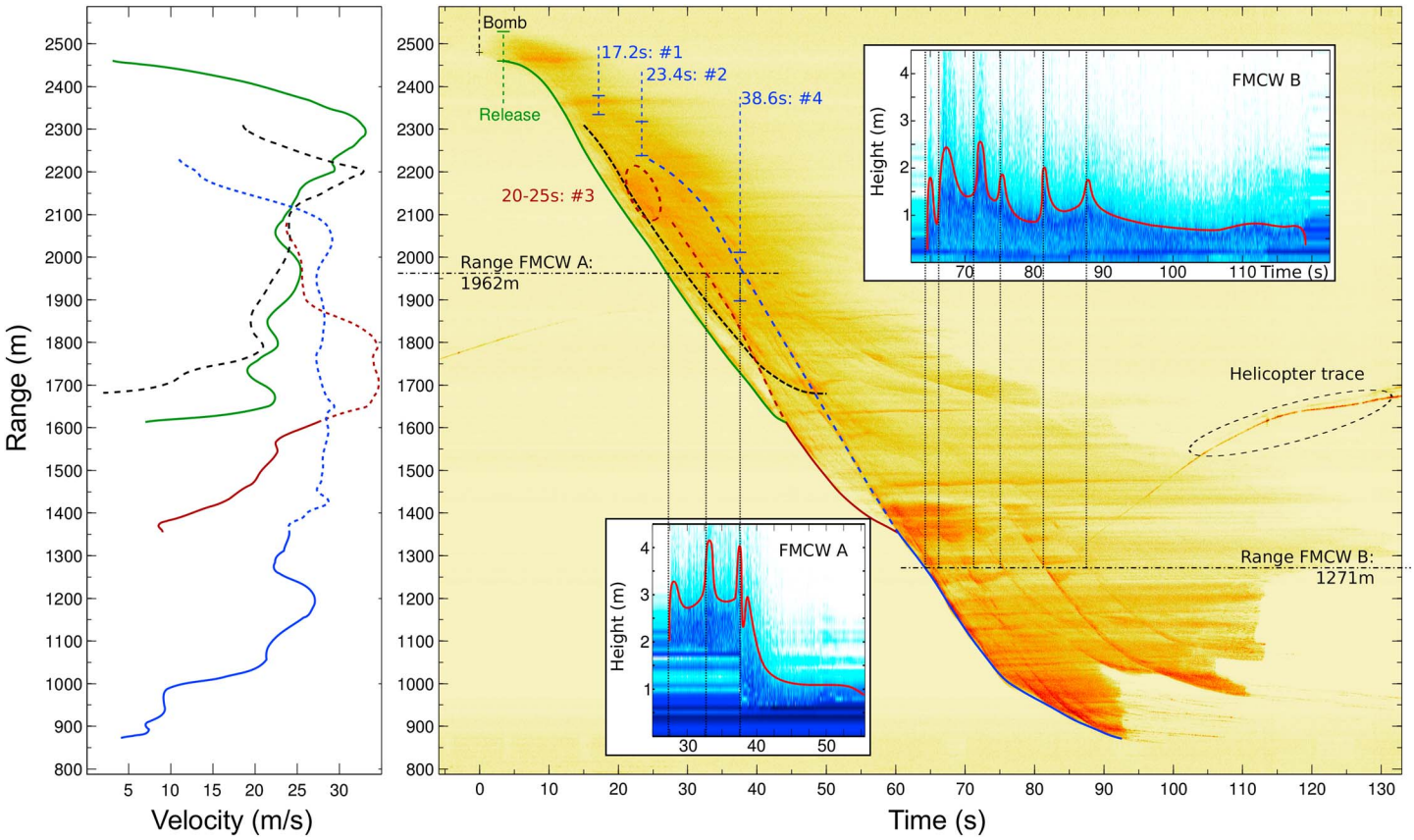

Figure 6. MTI image of avalanche #0019. Extent of slab releases (between the horizontal bars) and the resulting major surges (colored lines) are highlighted. (right) Small insets show the FMCW flow height measurements at caverns A and B, which connect well to the surges in the MTI. Note the abrupt erosion in FMCW A when the blue surge arrives. (left) Ground-parallel velocity $\dot{s}$ of surges along their talweg (solid lines = surges at the leading edge and dashed lines = surges inside the avalanche).

Note that feature #9 is a clear wave in the FMCW B data, but the corresponding features arrive in the MTI a few seconds earlier. Such a delay was most likely caused again by the location of the FMCW, which is around 20 m away from the channel axis. The avalanche stopped moving at 104 s according to the FMCW B signal, but GEODAR recorded still a weak signal until 115 s. This is presumably because the avalanche had stopped moving over FMCW B, but its narrow tail was still flowing in the bottom of the channel.

3.2. Generation and Evolution of Surges

The comparison with the upward looking FMCW radar has shown that the trajectories of surges we inferred from the GEODAR data correspond to variations in the flow depth. In this subsection we explore their generation and evolution.

3.2.1. Major Surges

Major surges were present in both avalanches #0019 and #0017. Avalanche #0019 had four major surges (Figure 6: green, black dashed, and red and blue lines), which overtook the foremost point of the avalanche one after the other. Avalanche #0017 contained at least one major surge, which always stayed several hundred meters behind the leading edge (Figure 3).

In order to identify the origin of the major surges, we compared the GEODAR data to the video and laser scan data (Figure 5). The video was used to locate surges at the lateral position and to infer the timing of the secondary releases if possible. The laser scan was used as complementary information to associate to each surge an origin and an initial release volume. Most of the major surges could be associated with secondary releases occurring along the avalanche path. The areas highlighted by black circles in the laser scan data (Figure 5) show the location of all secondary releases identified. The volume of secondary releases V_i can be even larger than the volume of the initial release V_0 (Table 1).

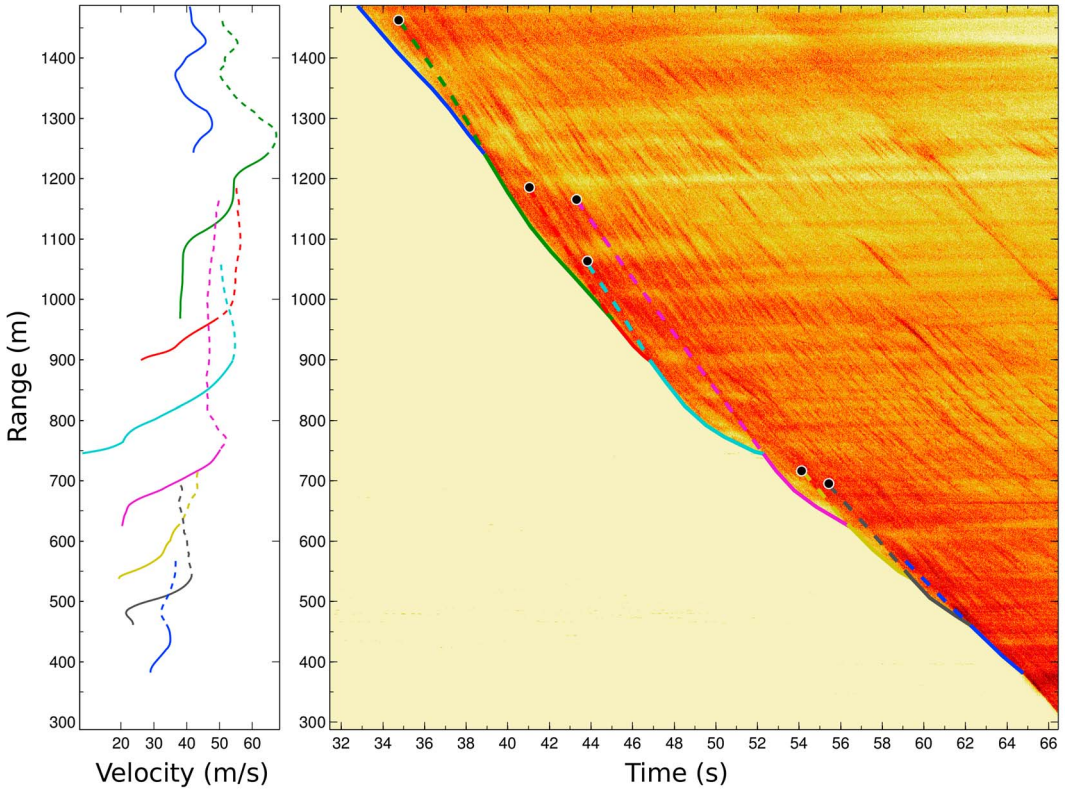

Figure 7. MTI image of avalanche #0017 (detail) from middle of channel down to deposit area below pylon. Surges overtake each other at the front. (right) Trajectories of surges are highlighted, start points for fitting procedure #3 marked with black dots. (left) Ground-parallel velocity of surges (solid lines = surges at the leading edge and dashed lines = surges inside the avalanche).

As an example we follow here the blue surge of avalanche #0019 from the origin to the deposit in greater detail (Figure 6). At time 17.2 s, slab #1 was released at around 2356 m range, while the leading edge (green) was already 150 m farther down. A short moment later, at 23.4 s, slab #2 was triggered just below slab #1 at an average range of 2280 m. Connecting both slabs in the space-time MTI plot reveals that the two together are reasonable candidates for causing the formation of the major surge marked in blue (Figure 6). Both secondary releases happened to the side of the main avalanche track, which meant that the acceleration was only driven by gravity. Eventually though, the slabs merged with the body of the main avalanche and started to accelerate attaining velocities beyond the front velocity (range <2100 m).

At 38.6 s the blue surge arrived at FMCW A (bottom left inset in Figure 6, right). The surge not only showed up as an increase in flow height change but also entrained instantaneously around 1 m from the old snow cover. *Sovilla et al.* [2006] characterized such instantaneous erosion as step entrainment, which is driven by the front of a surge. But the laser scan data (Figure 5) clearly show that the area #4 has a sharp boundary and suggests that a secondary release, the failure of a snow slab, happened. Presumably, the mass of slab #4 was incorporated into the blue surge, and it continued to travel with a relatively constant velocity. At a range of 1350 m, the leading edge was overtaken by the blue surge, and it is the blue surges which arrived at 64.5 s at cavern B as the new leading edge (top right inset in Figure 6, right). At the end of the steep channel (1000 m range), the blue surge started to decelerate and was then overtaken by several smaller surges. Note that the final runout of avalanche #0019 at 870 m range was due to this last released major surge.

We could observe that as soon as the leading edge is decelerating, its MTI amplitude is decreasing as well. Possibly, this decrease represents the starving of the surge as the flow height diminishes. Sometimes, the surges are still visible once they have been overtaken (Figure 6, black dashed). More often, however, they are not, either because they have merged with the surge that has overtaken them (Figure 1e) or because of losing mass and this may be a reason for its deceleration.

3.2.2. Minor Surges

Minor surges are observable in the lower part of avalanche #0017 and are shown in greater detail in Figure 7. These surges are visible especially in the avalanche head, the intermittent frontal region, and appear and disappear often, only existing for a few seconds. The leading edge of #0017 was overrun repeatedly by such minor surges coming from behind.

We believe that most minor surges come from a roll wave-like flow instability, and we are using *roll wave* to mean any variation in height and velocity that can develop from an initially uniform state [*Balmforth and Mandre*, 2004]. Some of them seem to start from terrain features, like curvature, bed roughness, or obstructions along the path since they started at the same range. For example, the MTI of avalanche #0017 (Figure 3) suggests that many minor surges start at the beginning of the channel at a range of around 1400 m and 1500 m. The MTI at this range shows slowly upward traveling broad features with high reflectance, which are maybe backward propagating hydraulic jumps with zero to negative phase velocities.

Some minor surges may have a very different mechanism: They may come from secondary slab releases or very rapid entrainment and perhaps be related to erosion-deposition waves [*Edwards and Gray*, 2015]. We have no direct evidence of this however.

It is a generic feature of shallow flows that they are unstable and develop instabilities when the Froude number exceeds a critical value. Close to this value, only small amplitude roll waves develop. Further from criticality, the previously mentioned slug flows and light flows can develop and these may be the cause of the intermittent frontal region. Instabilities of higher density clusters and rapid flow height variations are seen as the signature of this region in the avalanche flow [*Sovilla et al.*, 2015]. *Schaerer and Salway* [1980] reported an interval between those jets of 0.7 s to 1.4 s, which is very similar to the occurrence interval found in Figure 7. So these minor surges and the overrunning seem to be ubiquitous features of the intermittent frontal region. It is noteworthy that we do not see as many minor surges in the avalanche #0019, which was smaller, flowing more slowly and did not evolve the intermittent frontal region.

We estimated the Froude number as defined by $Fr = \dot{s}/\sqrt{gh\cos\theta}$ for the minor surges at the location of Cavern B ($\theta = 28.7°$) with velocity $\dot{s}$ and flow height h estimated from Figure 4. The Fr values are in the range of 4 to 9 with the majority of values around 6. The flows are highly supercritical and well above the 3.5 threshold for light flow. To prevent the occurrence of waves and instabilities, some stabilizing mechanisms are necessary. On the smallest scale this can be surface tension, whereas on a large scale it is internal dissipation. For a Newtonian fluid this corresponds to a Reynolds number criteria, but for non-Newtonian materials like snow it is more complicated though there has been some work in the direction of defining a critical Froude number [*Balmforth and Mandre*, 2004] which is found to be around 2, but factors like terrain roughness and topography can change this value.

The boundary between the dense core and the intermittent frontal region cannot be inferred from the GEODAR data; information about that only exists at the pylon. Unpublished data from the pylon suggest that avalanche #0017 has shortly after passing of the front a less than 50 cm shallow dense flow, but the density clusters as candidates for the minor surges reach up to 4 m above the sliding surface. In other data sets, minor surges are more often connected to the intermittent frontal region than to the dense core.

3.3. Velocity of Surges

The talweg for both avalanches are included in the VdlS overview (Figure 2) and, for comparison with the actual avalanche area, also in the laser scan data (Figure 5). The velocities were calculated by fitting a smoothing cubic spline to the talweg position $s(t)$ and differentiating the result to give $\dot{s}(t)$.

The velocities of the major surges in avalanche #0019 are shown in Figure 6 (left). This avalanche reached velocities up to 35 m s^{-1}. The green, red, and blue surges overtook the foremost position one after the other—effectively increasing the front velocity. The leading edge velocity is lower than the velocity of the surges traveling behind. At each overrun, the leading edge velocity is characterized by an abrupt discontinuity. These jumps can be larger than 10 m s^{-1}.

The minor surges in avalanche #0017 (Figure 7) reached velocities up to 60 m s^{-1}, overtaking the foremost position one after the other as did the major surges but more regularly and on a shorter time scale of around 3 s to 5 s. Numerous minor surges contributed to the leading edge. The overall leading edge velocity decreased from 50 m s^{-1} to around 30 m s^{-1} and was again lower than the velocity of the surges traveling behind.

In the steep channel (range >1000 m), overtaking seems to be the result of material from behind traveling faster than the leading edge (blue, green, and red lines in Figure 7) and catches up. Whereas in the beginning of the runout, where the slope is more gentle, the surges run with a similar velocity and overtake the leading edge when it rapidly decelerates. The resulting leading edge velocity is shown with the solid line in Figure 7, also with abrupt discontinuities. These jumps can be even larger than 10 m s^{-1} to 20 m s^{-1}.

Voellmy [1955] predicted and *Dent and Lang* [1983] reported that the leading edge velocity fluctuates around a mean front velocity even when slope is constant. They interpreted these fluctuations as surging or jetting (German *schiessend*), as parts from the avalanche body shot forward and overtake the leading edge. The overtaking of the leading edge shows that a simplistic model of an avalanche moving with a slowly varying velocity does not agree with the data as the front velocity is discontinuous.

4. Discussion

4.1. Slab Releases

Sovilla et al. [2006] observed with buried and upward looking FMCW radar that avalanches can entrain large amount of snow well behind the leading edge by a process which they called step entrainment. However, the GEODAR data in combination with the laser scan data suggest that this entrainment mechanism is not a process where the mass is entrained along an abrupt erosion front but rather due to the instantaneous failure of snow slabs. These secondary releases are located both inside and outside the avalanche track, and their failure is due to ground vibration, the avalanche motion, and weight initiating a new failure at a weak layer [*Schweizer et al.*, 2003]. These secondary releases can occur in front of or behind the leading edge, sometimes even hundreds of meters behind and beside the track.

The upper right inset of Figure 3 shows the detail of the release of slab #5 which was triggered in front of the leading edge. The corresponding video snapshot is found in Figure 5 (bottom left). Similar to the initial release, the avalanche signal in the GEODAR jumped instantaneous forward in range because the whole snow slab started moving at one moment in time. The radar signal of the young slab was weaker than neighbor signals of faster moving snow. Secondary releases failing inside the avalanche are therefore obscured by faster moving snow.

The laser scan data were used to reconstruct the mass balance of the avalanches. We estimated the initial released volume V_0, the volumes of the secondary releases V_i, and the total volume of snow entrained along the path V_t. In our case, we perform the volume balance only in the upper part of the track (> 1800 m range), because multiple avalanches influenced the snow cover change in the lower part. This area is also characterized by an average slope larger than 30°, and thus, errors in the erosion depth due to deposition are negligible [*Sovilla et al.*, 2010]. Table 1 summarizes the volume data and slab parameters. The volumes of the secondary releases V_i are in the same order of magnitude as the initial volume V_0. For avalanche #0019 V_i exceed the initial volume V_0 by a factor of 2, but in general V_i can exceed the initial volume many times.

We define an entrainment ratio v_e as the ratio between volume of gradual entrainment ($V_t - V_i$) and volume of secondary release (V_i) as

$$v_e = 1 - \sum_{i=0}^{n} \frac{V_i}{V_t}. \tag{4}$$

For avalanche #0017 we find that $v_e = 0.41$ and for #0019 $v_e = 0.53$. These numbers indicate that entrainment due to secondary released snow slabs is a dominant entrainment mechanism for these avalanches in respect to other entrainment like plowing or abrasion [*Gauer and Issler*, 2004].

Furthermore, the average erosion depth $d_i = V_i/A_i$ of the secondary releases can be much higher than the erosion depth around these slabs, e.g., for slab #7 $d_i = 1.9$ m while outside the slab only 0.5 m of snow was entrained (Figure 5). We see also that some of the largest fracture depth of up to 6 m correspond to slabs which started below rock faces. We think that such large snow accumulations were build up by frequent sluff flows after snowfall events of the steep rock faces.

The instantaneous release and the large erosion depth may lead to a major surge where the mass runs concentrated as a confined surge. If they start on different talwegs, they start as a separate avalanche and later join the original avalanche and become a major surge. The data show that they can be long in respect to the

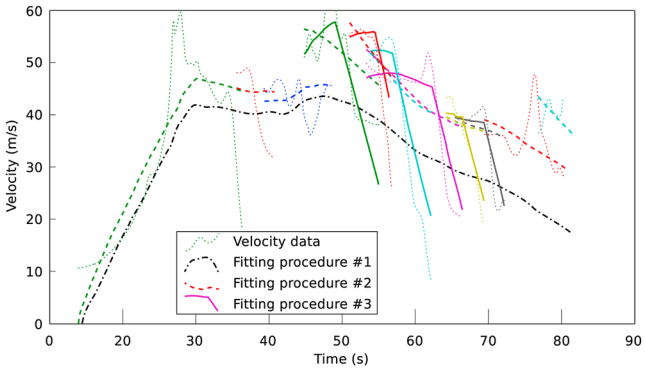

Figure 8. Point-mass model optimization of position data $s(t)$ from avalanche #0017 but displayed as velocities (measurements = thin dotted lines). Black dash-dotted line results from the simulation on the avalanches leading edge (FP #1). Colored dashed lines describe the same trajectories but allow each surge an initial velocity E_i and start position s_0 (FP #2). Solid colored lines are optimization runs of FP #3 on surge position inside the avalanche (flat part) and at leading edge position (steep deceleration).

total runout of the original avalanche, so they keep their identity for a long time. The major surges can contain similar, or even more, mass than the original release thus resulting in a much longer and uneven distribution of entrained snow along the full avalanche flow.

It is clear that secondary releases and slab failures are governed by the overall stability of the snowpack. The two avalanches presented here are having both the same quite unfavorable snowpack [*SLF*, 2015], and as we showed, secondary releases are an important entrainment contribution to the avalanche flow. Estimating this importance of secondary release for other snowpack conditions will require further avalanche observations combined with data on the snowpack stabilities [*Schweizer et al.*, 2003].

4.2. Effective Friction

A detailed comparison of our data with 2-D avalanche simulations is beyond the scope of this paper, and also, for the reasons we now set out, likely to show poor agreement. Instead, we analyze the talweg trajectories $s(t)$ of avalanche #0017's minor surges by calculating their effective friction. We use the point-mass model (equation (5)), which can be thought of as a zeroth-order shallow water Voellmy-Salm model or more precisely as a centre-of-mass model like the PCM model developed by *Perla et al.* [1980] since we neglect the flow height. This procedure can be thought of a physically based smoothing of the surge velocities, since numerical differentiation of data is poorly conditioned.

This model balances inertia with gravitational acceleration, Coulomb friction term, and a velocity-squared drag term, so that

$$\ddot{s} = g\sin\theta - \mu g\cos\theta - \lambda\dot{s}^2\,, \tag{5}$$

where $\theta(s)$ is the local slope angle, μ is the friction coefficient, and λ is a dynamic drag coefficient with dimensions of inverse length. Note that $\lambda = \frac{g}{\xi h}$ in the Voellmy-Salm approach. By changing variables to kinetic energy per unit mass $E = \dot{s}^2/2$ and writing $\ddot{s} = \mathrm{d}E/\mathrm{d}s$ the equations can be directly integrated once to get

$$E(s) = E_0 e^{\lambda(s_0 - s)} + \int_{s_0}^{s} g\left[\sin\theta(r) - \mu\cos\theta(r)\right] e^{\lambda(r-s)}\,\mathrm{d}r, \tag{6}$$

with E_0 as initial energy and s_0 as the start position. The energy $E(s)$ can then be used to calculate the relationship between time t and position s as

$$t = \int_{s_0}^{s} \frac{1}{\sqrt{2E(s)}}\mathrm{d}s\,. \tag{7}$$

The parameters μ and λ in equation (6) are found by minimizing the least squares error between the talweg position $s(t)$ and the model output. To constrain μ and λ well, there must be a reasonable variation in velocity $\dot{s}(t)$, which is not the case for most of the trajectories. However, these smoothed trajectories are still valid and we do not directly consider μ and λ but simply regard these as parameters in a smoothing procedure along with E_0. Instead, we directly look at the total effective friction defined as

$$\mu_e(s) = \tan\theta - \frac{\ddot{s}}{g\cos\theta} = \mu + \frac{\lambda v(s)^2}{g\cos\theta(s)}\,, \tag{8}$$

where $v(s)$ is evaluated from the fitted parameters (E_0, λ, μ) with equation (6). We run three different fitting procedures (FP) to compare with each other, and the resulting modeled velocities are shown in Figure 8 with different line styles. The effective friction $\mu_e(s)$ is shown as a function of velocity $v(s)$ in Figure 9.

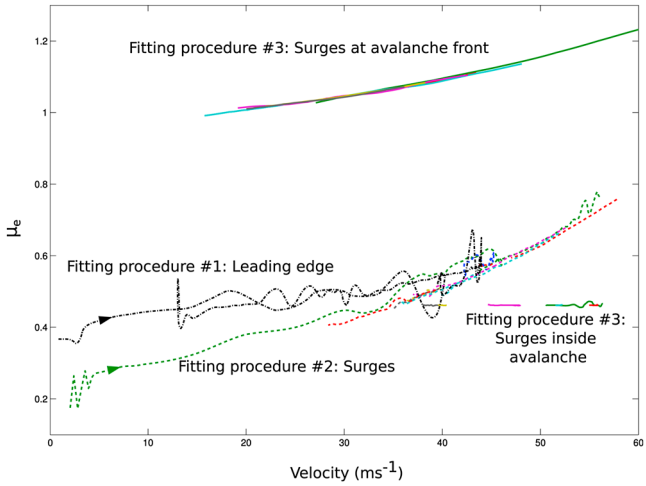

Figure 9. Effective friction μ_e as a function of the velocity $\dot{s}$ for the same data as Figure 8. The curves are multivalued because the velocity in general increases and decreases in time, but the arrows indicate the direction from initiation to deposit. The black dash-dotted line shows the leading edge optimization (FP #1). The dashed curves give similar values, which represent the optimization of the surges with one set of friction (FP #2). The relationship $\mu_e(\dot{s})$ for FP #1 and FP #2 is velocity-squared dependent. The two regions with solid lines (FP #3) give $\mu_e \approx 0.44$ for surges inside and $\mu_e > 1$ at the front of the flow.

Fitting Procedure #1. The black dash-dotted line describes the descent of the whole avalanche as a result from optimizing to the foremost point of the leading edge position data only. The velocity is always underestimated, although the overall velocity trends are followed, that is, initial acceleration (<30 s), steady state, acceleration at the beginning of the channel (40 s to 45 s), and deceleration in the runout area (>50 s). This model run represents what is captured by existing models, and we will call the derived friction value as apparent friction μ_a because the full evolution of the avalanche's leading edge is tried to be represented by one set of μ and λ values.

Fitting Procedure #2. Similar friction values are obtained when optimizing every surge position (dashed colored lines). Since each surge has a different initial velocity, each trajectory starts with an individual initial energy E_i. The optimization was used to find a common friction coefficient μ and λ for all surges while allowing freedom in E_i. This model run describes the velocity data better but does not capture the dramatic deceleration of the surges.

Fitting Procedure #3. The thick colored lines show the model run on the position data of the most obvious surges. We limited the analysis on the most pronounced minor surges in the range of channel 1 (1400 m to 1000 m) and the beginning of the runout (1000 m to 500 m), to be sure that these surges were running on top of each other (Figure 1e). In contrast to the prior simulation, the talweg trajectories $s(t)$ were split into two parts: in the avalanche body and at the leading edge. For each part a set of friction parameters were optimized. The first set describes the surges inside the avalanche body; they move faster than the leading edge and thus having low effective friction μ_e. The second set describes them as soon they overtake the leading edge; they dramatically decelerate and have a very high effective friction μ_e. This additional freedom results in a good description of the surges deceleration.

The effective friction for FP #1 and FP #2 gives a similar value of μ_e which lies in between 0.3 and 0.7 depending on the velocity squared (Figure 9). For FP #3 we obtain two friction parameters: for the surges inside the avalanche body $\mu_e = 0.44$ and for the deceleration of the surges after they overtook the leading edge a much higher friction $\mu_e = 1$ to 1.2. These values reflect our hypothesis that the effective friction has to be very different between the front and the body of the avalanche to yield the observed velocities. Similar results are found by *Gauer et al.* [2007] with Doppler radar measurement where they obtain the retarding acceleration (equivalent to μ_e here) of fictitious mass blocks behind the front. The mass blocks show fluctuating retarding accelerations, which they interpret as surging and describe it as a "stop and go" movement. There are a variety of effects that could cause this observation, which we now discuss.

Entrainment. If snow is entrained, then it must be accelerated leading to an increased effective friction. This will mainly slow down the front, where FMCW radar suggests that the majority of mass is entrained. In addition, there may also be enhanced drag due to plowing effects. Certainly, entrainment is extremely important and can have a large effect on flow dynamics in general [*Sovilla et al.*, 2006]. Later, flowing avalanches are possibly entraining older deposits instead of fresh snow. Avalanche #0017 was the second avalanche on this day.

Surface Smoothing. The initial snow surface may be rough and results in high friction. A rough surface, e.g., old deposits, can easily be smoothed out by the snow running over it, thus removing obstructions and filling in gaps.

Surface Melting. Energy dissipation in the shear layer may cause the interface to melt. Not only will this result in an extremely smooth surface but Coulomb friction may also disappear altogether and be replaced by a viscous lubrication layer. This effect has been estimated in *Kern et al.* [2004] and undoubtedly happens in some avalanches, but here the flow temperatures were everywhere below −5°C.

Height Changes. This trajectory analysis neglects the effects of flow depth changes. Deeper flows will typically experience reduced effective friction. If the front loses mass, due to deposition or starving, then it will experience higher effective friction.

Internal Flow Structure. The flow may have a different structure near the front where there are strong height gradients, which could influence the effective friction.

Probably all of the mechanisms play some role some of the time. Other mechanisms have been proposed in literature to explain the reduction of effective friction such as fluidization and lubrication (see *Johnson et al.* [2016] for a review of some of these). These ones are all smooth, however, and do not give the two distinct regimes that we see nor do they explain the extremely high values. In contrast, we propose mechanisms which are possibly suitable to change dramatically as soon as the minor surge reaches and overtakes the leading edge.

Salm and Gubler [1985] and *Ancey and Meunier* [2004] investigate the velocity dependency of the retarding forces as a result of changes in the flow regime. They distinguish between pure Coulomb friction where the drag coefficient $\lambda = 0$ diminishes and a velocity-dependent regime where the retarding force $F_{\mathrm{ret}} \propto \dot{s}^n$ is proportional to the velocity. While *Ancey and Meunier* [2004] could not find a universal exponent n, *Salm and Gubler* [1985] choose $n = 1$ for partly fluidized regimes and $n = 2$ for fully fluidized regimes. The slight curvature in Figure 9 suggests that $n = 2$ is reasonable for the leading edge and also for individual surges. Nearly all dry granular flow models [*Forterre and Pouliquen*, 2008] have only a very weak dependence of friction on velocity, i.e., $n = 0$ for large v, but there is experimental evidence [*Holyoake and McElwaine*, 2012] for $n = 2$ for large v. However, our data suggest that the friction parameters must be radically changed depending on whether the surge is at the leading edge of the avalanche or is internal in order to capture the overtaking and slowing of the surges.

This difference may be an explanation of why friction coefficients necessary to produce observed runouts are typically much lower than those measured in small-scale snow experiments. These small chute experiments can be thought as only one single surge, whereas a real avalanche can comprise many minor surges. The more surging occurs, the longer the runout will be as internal surges can keep a high velocity.

Current avalanche models reflect the motion of the leading edge and not the underlying motion of surges. This is what the fitting procedure #1 represents. The models are therefore based on choosing an approximation to the apparent friction μ_a for the descent of the leading edge from release to deposit. In this approach longer runouts can only come from lower apparent friction μ_a values. The guidelines, provided to avalanche practitioners, say that larger avalanches, in the sense of volume and runout, should be modeled with lower μ_a friction values [*Bartelt et al.*, 1999]. While this may be useful for practical purposes, it is unsatisfactory from a scientific point of view. We propose that a possible explanation lies with an increase in surging in larger avalanches with a more rapid change over of material in the head. If we compare the dynamics of both presented avalanches at the beginning of the deposit zone for ranges smaller than 1000 m, the smaller one (#0019, Figure 6) showed nearly no surging and starved shortly afterward at 900 m range, whereas the larger one (#0017, Figure 3) was able to continue with an overall high velocity of 30 m s^{-1} (Figure 7), and the deposits extended into the valley ground. The video data and the FMCW radars suggest that avalanche #0019 did not develop a substantial intermittent frontal region, while the bigger avalanche #0017 did (Figure 4).

5. Conclusion

In this paper we have analyzed data from artificially released avalanches observed at the Vallée de la Sionne test site. We combined data from high-resolution video cameras, laser scan, FMCW radar, and the GEODAR system. We showed that line features in the GEODAR data correspond to flow height variations or more precisely to surges in the denser part that is the intermittent frontal region as well as the dense flowing core

of the avalanche. The GEODAR data let us track these surges even when they are optically obscured by the powder cloud.

By identifying lines in the GEODAR data and mapping them onto the terrain we show that large avalanches are composed of many, largely independent surges. The largest of these surges originate from secondary slab releases inside and beside the avalanche track, which can increase the mass of an avalanche many times. These major surges can be tracked over the entire avalanche path and frequently move much faster than the front and overtake it. Usually, in simulations all materials in the starting zone are assumed to start simultaneously and secondary release is not considered. Our data show, however, that this can be far from the truth, and the mass distribution in the avalanche may be very different resulting in changed dynamics and runout.

The smaller surges appear to be clusters of denser material or roll wave-like instabilities that occur in the dense or intermittent frontal region of larger avalanches. Again, these surges can move faster than the leading edge velocity and therefore frequently overtake the leading edge. The minor surges we focus on in this work show very different friction parameters in comparison to the overall avalanche motion. They exhibit lower effective friction inside the avalanche but much higher effective friction once they reach the leading edge which causes a rapid deceleration. Frontal entrainment, surface smoothing, and surface melting are all possible mechanisms which can result in such behavior each of which may be significant in some situations.

One key conclusion of this work is that the average behavior of the avalanche's leading edge does not accurately represent the underlying flow. The velocities of internal surges can be significantly larger than the average leading edge velocity due to reduced internal friction, suggesting that current models most likely underestimate the dynamic forces that the internal flow of avalanches can cause on structures. Since the differential appears to grow with avalanche size, surging is a possible candidate to explain why lower averaged friction parameters are typically required to back calculate larger avalanches. To correctly represent these phenomena, models must be developed that include the physical evolution of the basal surface as well as the effects of surging with changing effective friction between inside and the leading edge of the avalanche.

Acknowledgments

Data are available upon request to the corresponding author. The research was funded by the Swiss National Science Foundation (SNSF) project "High Resolution Radar Imaging of Snow Avalanches," grant 200021_143435, and the test site and infrastructure by SNSF R'EQUIP project "Snow Avalanches in the Swiss experiment," grant 206021_113069/1, and the canton of Valais. Special thanks are due to our colleagues at the electronics and workshop of SLF for their invaluable support. We are grateful to three anonymous reviewer for their valuable comments which increase the clarity and quality of this paper.

References

Ammann, W. J. (1999), A new Swiss test-site for avalanche experiments in the Vallée de la Sionne/Valais, *Cold Reg. Sci. Tech.*, *30*(1), 3–11, doi:10.1016/S0165-232X(99)00010-5.

Ancey, C. (2006), *Dynamique des Avalanches et Gestion du Risque*, Presses Polytech. Univ. Romandes–Cemagref editions, Lausanne, Switzerland.

Ancey, C., and M. Meunier (2004), Estimating bulk rheological properties of flowing snow avalanches from field data, *J. Geophys. Res.*, *109*, F01004, doi:10.1029/2003JF000036.

Ash, M., P. V. Brennan, K. Chetty, J. N. McElwaine, and C. Keylock (2010), FMCW radar imaging of avalanche-like snow movements, in *Proceedings of the 2010 IEEE Radar Conference*, pp. 102–107, IEEE, Arlington, Va., doi:10.1109/RADAR.2010.5494643.

Ash, M., P. V. Brennan, C. J. Keylock, N. M. Vriend, J. N. McElwaine, and B. Sovilla (2014), Two-dimensional radar imaging of flowing avalanches, *Cold Reg. Sci. Tech.*, *102*, 41–51, doi:10.1016/j.coldregions.2014.02.004.

Ash, M. J., P. V. Brennan, N. M. Vriend, J. N. McElwaine, and C. J. Keylock (2011), Two-dimensional FMCW radar imaging of entire avalanche events, in *5th IASME/WSEAS International Conference on Geology and Seismology (GES '11)*, pp. 153–157, WSEAS, Cambridge, U. K.

Balmforth, N. J., and S. Mandre (2004), Dynamics of roll waves, *J. Fluid Mech.*, *514*, 1–33, doi:10.1017/S0022112004009930.

Bartelt, P., M. Christen, U. Gruber, and D. Issler (1999), *Neue Berechnungsmethoden in der Lawinengefahrenkartierung*, WSL Institute for snow and avalanche research SLF, Davos Dorf, Switzerland.

Carroll, C., M. Louge, and B. Turnbull (2013), Frontal dynamics of powder snow avalanches, *J. Geophys. Res. Earth Surf.*, *118*, 913–924, doi:10.1002/jgrf.20068.

Corripio, J. G. (2004), Snow surface albedo estimation using terrestrial photography, *Int. J. Remote Sens.*, *25*(24), 5705–5729, doi:10.1080/01431160410001709002.

Dent, J., and T. Lang (1983), A biviscous modified Bingham model of snow avalanche motion, *Ann. Glaciol.*, *4*, 42–46.

Eckert, N., C. Keylock, D. Bertrand, E. Parent, T. Faug, P. Favier, and M. Naaim (2012), Quantitative risk and optimal design approaches in the snow avalanche field: Review and extensions, *Cold Reg. Sci. Tech.*, *79*, 1–19.

Edwards, A. N., and J. M. N. T. Gray (2015), Erosion-deposition waves in shallow granular free-surface flows, *J. Fluid Mech.*, *762*, 35–67.

Forterre, Y., and O. Pouliquen (2008), Flows of dense granular media, *Annu. Rev. Fluid Mech.*, *40*, 1–24.

Gauer, P., and D. Issler (2004), Possible erosion mechanisms in snow avalanches, *Ann. Glaciol.*, *38*, 384–392, doi:10.3189/172756404781815068.

Gauer, P., M. Kern, K. Kristensen, K. Lied, L. Rammer, and H. Schreiber (2007), On pulsed doppler radar measurements of avalanches and their implication to avalanche dynamics, *Cold Reg. Sci. Tech.*, *50*, 55–71, doi:10.1016/j.coldregions.2007.03.009.

Gubler, H., and M. Hiller (1984), The use of microwave FMCW radar in snow and avalanche research, *Cold Reg. Sci. Tech.*, *9*(2), 109–119, doi:10.1016/0165-232X(84)90003-X.

Hallikainen, M., F. Ulaby, and M. Abdelrazik (1986), Dielectric properties of snow in the 3 to 37 GHz range, *IEEE Trans. Antennas Propag.*, *34*(11), 1329–1340.

Henderson, F. M. (1966), *Open Channel Flow*, Macmillan, New York.

Holyoake, A. J., and J. N. McElwaine (2012), High-speed granular chute flows, *J. Fluid Mech.*, *710*, 35–71.

Hopfinger, E. J. (1983), Snow avalanches motion and related phenomena, *Annu. Rev. Fluid Mech.*, *15*, 47–96.

Issler, D., et al. (2005), A comparison of avalanche models with data from dry-snow avalanches at Ryggfonn, in *Landslides and Avalanches ICFL 2005 Norway*, edited by D. Issler et al., pp. 173–180, Taylor and Francis Ltd., London.

Johnson, B. C., C. S. Campbell, and H. J. Melosh (2016), The reduction of friction in long runout landslides as an emergent phenomenon, *J. Geophys. Res. Earth Surf.*, *121*, 881–889, doi:10.1002/2015JF003751.
Kern, M. A., F. Tiefenbacher, and J. N. McElwaine (2004), The rheology of snow in large chute flows, *Cold Reg. Sci. Tech.*, *39*(2-3), 181–192, doi:10.1016/j.coldregions.2004.03.006.
Lundberg, A., C. Richardson-Näslund, and C. Andersson (2006), Snow density variations: Consequences for ground-penetrating radar, *Hydrol. Process.*, *20*(7), 1483–1495, doi:10.1002/hyp.5944.
McElwaine, J. N. (2003), Filming avalanches, SATSIE Rep. Dep. of Applied Mathematics and Theoretical Physics, Univ. of Cambridge, Cambridge, U. K.
Pérez-Guillén, C., B. Sovilla, E. Suriñach, M. Tapia, and A. Köhler (2015), Deducing avalanche size and flow regimes from seismic measurements, *Cold Reg. Sci. Tech.*, *121*, 25–41, doi:10.1016/j.coldregions.2015.10.004.
Perla, R., T. T. Cheng, and D. M. McClung (1980), A two-parameter model of snow avalanche motion, *J. Glaciol.*, *26*(94), 197–207.
Rammer, L., M. A. Kern, U. Gruber, and F. Tiefenbacher (2007), Comparison of avalanche velocity measurements by means of pulsed Doppler radar, continuous wave radar and optical methods, *Cold Reg. Sci. Tech.*, *50*(1–3), 35–54, doi:10.1016/j.coldregions.2007.03.014.
Rastello, M., F. Rastello, H. Bellot, F. Ousset, F. Dufour, and L. Meier (2011), Size of snow particles in a powder-snow avalanche, *J. Glaciol.*, *57*(201), 151–156.
Rignot, E., K. Echelmeyer, and W. Krabill (2001), Penetration depth of interferometric synthetic-aperture radar signals in snow and ice, *Geophys. Res. Lett.*, *28*(18), 3501–3504.
Salm, B., and H. Gubler (1985), Measurement and analysis of the motion of dense flow avalanches, *Ann. Glaciol.*, *6*, 26–34.
Schaerer, P., and A. Salway (1980), Seismic and impact-pressure monitoring of flowing avalanches, *J. Glaciol.*, *26*, 179–187.
Schweizer, J., J. Bruce Jamieson, and M. Schneebeli (2003), Snow avalanche formation, *Rev. Geophys.*, *41*(4), 1016, doi:10.1029/2002RG000123.
Sovilla, B., P. Burlando, and P. Bartelt (2006), Field experiments and numerical modeling of mass entrainment in snow avalanches, *J. Geophys. Res.*, *111*, F03007, doi:10.1029/2005JF000391.
Sovilla, B., J. N. McElwaine, M. Schaer, and J. Vallet (2010), Variation of deposition depth with slope angle in snow avalanches: Measurements from Vallée de la Sionne, *J. Geophys. Res.*, *115*, F02016, doi:10.1029/2009JF001390.
Sovilla, B., J. McElwaine, W. Steinkogler, M. Hiller, F. Dufour, E. Suriñach, C. P. Guillen, J.-T. Fischer, E. Thibert, and D. Baroudi (2013), The full-scale avalanche dynamics test site Vallée de la Sionne, in *International Snow Science Workshop, Grenoble–Chamonix Mont-Blanc*, Grenoble, France.
Sovilla, B., J. N. McElwaine, and M. Y. Louge (2015), The structure of powder snow avalanches, *C. R. Phys.*, *16*(1), 97–104, doi:10.1016/j.crhy.2014.11.005.
Sovilla, B., T. Faug, A. Köhler, D. Baroudi, J.-T. Fischer, and E. Thibert (2016), Gravitational wet avalanche pressure on pylon-like structures, *Cold Reg. Sci. Tech.*, *126*, 66–75.
Swiss Geoportal (2015), Federal Office of Topography, Wabern, Switzerland. [Available at https://map.geo.admin.ch/?topic=ech&X=127547.50&Y=594372. 50&zoom=8, accessed: 30 September 2015.]
Te Chow, V. (1959), *Open Channel Hydraulics*, McGraw-Hill Book Company Inc., New York.
Turnbull, B., J. N. McElwaine, and C. J. Ancey (2007), The Kulikovskiy-Sveshnikova-Beghin model of powder snow avalanches: Development and application, *J. Geophys. Res.*, *112*, F0100, doi:10.1029/2006JF000489.
Voellmy, A. (1955), Über die Zerstörungskraft von Lawinen, *Schweizerische Bauzeitung*, *73*(15), 212–217.
Vriend, N. M., J. N. McElwaine, B. Sovilla, C. J. Keylock, M. Ash, and P. V. Brennan (2013), High resolution radar measurements of snow avalanches, *Geophys. Res. Lett.*, *40*, 727–731, doi:10.1002/grl.50134.
WSL Institute for Snow and Avalanche Research SLF (2015), Weekly Snow and Avalanche Report: 30 January – 5 February 2015, Tech. Rep., WSL Institute for snow and avalanche research SLF, Davos Dorf, Switzerland. [Available at http://www.slf.ch/schneeinfo/wochenbericht/2014-15/0130/index_DE.]